



Unveiling the origin of boosted photocatalytic hydrogen evolution in simultaneously (S, P, O)-Codoped and exfoliated ultrathin g-C₃N₄ nanosheets

Qinqin Liu^a, Jiyou Shen^a, Xiaohui Yu^a, Xiaofei Yang^{b,*}, Wei Liu^a, Juan Yang^a, Hua Tang^{a,*}, Hui Xu^c, Huaming Li^c, Youyong Li^d, Jingsan Xu^{e,*}

^a School of Materials Science and Engineering, Engineering Institute of Advanced Manufacturing and Modern Equipment Technology, Jiangsu University, Zhenjiang, Jiangsu, 212013, PR China

^b College of Science, Institute of Materials Physics and Chemistry, Nanjing Forestry University, Nanjing, 210037, PR China

^c Institute for Energy Research, School of the Environment and Safety Engineering, Jiangsu University, Zhenjiang 212013, PR China

^d Institute of Nanoscience and Technology, Soochow University, Soochow 215000, PR China

^e School of Chemistry, Physics and Mechanical Engineering, Queensland University of Technology, Brisbane, QLD 4001, Australia

ARTICLE INFO

Keywords:

g-C₃N₄

2D materials

Nonmetal co-doping

Photocatalytic hydrogen evolution

ABSTRACT

Recently, metal-free graphitic carbon nitride (g-C₃N₄) has been recognized as a potential candidate for high-performance photocatalytic hydrogen production while challenges still remain due to poor electronic properties and limited surface active sites. We demonstrate that g-C₃N₄ can be simultaneously co-doped with S, P and O nonmetal-atoms and exfoliated into ultrathin 2D nanosheets with a thickness of ~3 nm by a simple, sequential thermal synthesis. The multi-atoms doping and nanostructure modulation remarkably enhanced the photocatalytic hydrogen production under illumination, with the optimal H₂ evolution rate reaching 2480 μmol g⁻¹ h⁻¹. First-principle calculations and experimental evidences suggest that, upon elemental doping within the g-C₃N₄ framework, S atoms occupied the interstitial sites and P and O atoms replaced the C and N atoms, respectively. Consequently, photo-induced charge transfer and separation significantly improved owing to the construction of a more favorable charge transfer pathway. Furthermore, introducing heteroatoms into the structure of g-C₃N₄ narrowed the bandgap and negatively shifted the conduction band edge, leading to extended visible-light absorption and stronger electron reducibility for subsequent H₂ production. Importantly, the in-situ generated 2D g-C₃N₄ nanosheets exhibited more catalytic surface sites, which was highly beneficial to the photocatalytic water splitting.

1. Introduction

Photo-splitting water into hydrogen by semiconducting photocatalysts is considered as an effective approach to alleviate the modern energy crisis [1–6]. Among various visible-light-driven photocatalysts, metal-free polymeric graphitic carbon nitride (g-C₃N₄) has attracted huge interest due to its suitable band structure for hydrogen production reaction (HER), high thermal and chemical stability as well as low cost [7–17]. However, for practical application, pristine g-C₃N₄ suffers from fast recombination of photogenerated carriers, low surface area and low density of active sites [18–21]. In this context, a number of strategies have been developed to solve these drawbacks and improve the photocatalytic activity of g-C₃N₄. One approach is to dope g-C₃N₄ with heteroatoms, such as metal atoms and non-metal atoms [22–24].

Compared with other modification approaches such as constructing heterojunction photocatalysts and morphology engineering, elemental doping is of particular interest because it can modify the electrical and optical properties g-C₃N₄ from an atomic level, such as tuning the band structures, narrowing the optical bandgaps and improving charge transport [25–27].

Numerous studies have been conducted for non-metal doping of g-C₃N₄. For instance, Zou et al. introduced boron atoms into the C sites of g-C₃N₄ and demonstrated that boron doping effectively improved the photo-degradation activity [28]. Wang et al. observed that fluorine doping mainly resulted in C–F bonding in the framework and led to narrowed bandgap and thus extended light-absorption range [29]. First-principles theoretical study demonstrated that atoms preferentially substituting for the edge C and N atoms are located at the

* Corresponding authors.

E-mail addresses: xiaofei.yang@njfu.edu.cn (X. Yang), huatang79@163.com (H. Tang), Jingsan.Xu@qut.edu.au (J. Xu).

<https://doi.org/10.1016/j.apcatb.2019.02.020>

Received 23 December 2018; Received in revised form 28 January 2019; Accepted 9 February 2019

Available online 11 February 2019

0926-3373/ © 2019 Elsevier B.V. All rights reserved.

interstitial sites of in-planar g-C₃N₄, thereby modulating the optical and electronic properties of g-C₃N₄ [30]. The majority of previous reports are focused on mono-element doping, however, the simultaneous doping of two kinds of non-metal atoms into g-C₃N₄ such as (P, S) co-doping [31], (P, Na) co-doping [32] and (C, O) co-doping [33] has been demonstrated to show higher photocatalytic activity and unusual physiochemical characteristics in comparison with single element doping. It has been revealed that doping site is crucial for the photocatalytic performance of g-C₃N₄ [34]. Therefore, it is demanding to carry out multi-element doping in the g-C₃N₄ matrix and explore the mechanism on the doping-induced enhancement of photocatalytic activity.

Alternatively, the photocatalytic activity of g-C₃N₄ can be improved by exfoliation of the bulk materials into nanosheets, taking advantage of the layered structure of g-C₃N₄ with increased surface area and more exposed active sites [35]. Typically, g-C₃N₄ exfoliation is conducted by an ultrasound-assisted liquid process, producing nanosheets with lateral sizes up to 100 nm [36]. To further decrease the size of the nanosheets, hydrothermal treatments and/or chemical etching can be applied, which cuts the g-C₃N₄ into quantum dots with an average diameter below 10 nm [37]. Ultrathin g-C₃N₄ nanosheets can also be generated by thermal-assisted exfoliation process. These exfoliated 2D g-C₃N₄ nanosheets exhibit significantly enhanced photoresponse compared to the bulk counterpart [38].

Herein, we report the simultaneous (S, P, O) doping and exfoliation of g-C₃N₄ into ultrathin 2D nanosheets by a simple annealing method. Firstly, S and P doped g-C₃N₄ (noted as CN-SP) was synthesized through thermal condensation of mixed precursors of melamine, thiourea and diammonium phosphate. After that, the as-obtained CN-SP was annealed in air for O doping and concurrently the material was exfoliated into ultrathin, flat nanosheets with a thickness of ~3 nm (noted as CN-SPO). The CN-SPO nanosheets exhibited larger surface area associated with increased active sites, modulated band structure, enhanced charge transport upon photo-excitation, leading to significantly improved photocatalytic hydrogen evolution. Under optimized condition, the H₂ evolution rate over the CN-SPO nanosheets reached 2480 $\mu\text{mol g}^{-1} \text{h}^{-1}$, which is 5 times higher than pristine g-C₃N₄. The mechanism for the photoactivity enhancement through doping processes was explored by DFT calculations in combination with a series of experimental tests.

2. Experimental methods

2.1. Preparation of doped g-C₃N₄

Melamine is used as a precursor for g-C₃N₄ (referred as CN), and the doping sulfur or phosphorus is supplied by thiourea and ammonium phosphate, respectively. First of all, x g of (NH₄)₂HPO₄ (x = 0, 0.5, 1, 2, 3) was dissolved in 50 mL deionized water. Then, 1 g thiourea was dissolved to the above solution, subsequently, 10 g melamine was dispersed. After that, the excess water in the whole slurry was removed via evaporation. Afterwards, the resultant solids were heated at 550 °C for 4 h with a heating rate of 2 °C/min. The resultant products were successively labeled as CN-SP 0.5, CN-SP, CN-SP 2 and CN-SP 3. Similarly, CN-S and CN-P were fabricated using the same procedure without adding ammonium phosphate or thiourea, respectively. For preparing oxygen doped CN-SP sample, CN-SP powders were further heat treated via the secondary and the third pyrogenation at 550 °C for 1 h with a heating rate of 5 °C/min and the as-obtained sample was named as CN-SPM and CN-SPO, respectively.

2.2. Characterization

The powder X-ray diffraction (XRD) patterns were obtained using Bruker D8 advance X-ray diffractometer at room temperature using Cu K α (λ = 0.15406 nm). Infrared spectrometer (FT-IR) was carried out on the Nicolet company Nicolet Nexus 470. The specific surface area was

determined by the multipoint Brunauer-Emmett-Teller (BET) method on NETZSCH NOVA3000e. The morphology of the products was observed via scanning electron microscopy (SEM, JEOL JXA-840A) and transmission electron microscopic (TEM, Japan JEM-100CX II100 kV). X-ray photoelectron spectrum (XPS) was characterized by PHI-5000C system. UV-vis diffused reflectance spectra were recorded using a UV-vis spectrophotometer (UV2550, Japan Shimadzu). Fluorescence spectrophotometer (Hitachi, F-7000) and electrochemical workstation (Chenhua Instruments, CHI660D) with a three electrode system were used to record the Photoluminescence (PL) spectra, photocurrent response and EIS Nyquist plots. The electron spin resonance (ESR) measurements were carried out at X-band frequency on a Bruker A300 spectrometer with 2,2,6,6-Tetramethylpiperidine-1-oxyl (TEMPO) radical capture reagent. Typically, the photocatalyst (0.10 g) was added to a NaHCO₃ aqueous solution (for TEMPO-e⁻ signal) or acetonitrile solution (for TEMPO-h⁺ signal) containing TEMPO (0.05 mM) within a container. After deoxygenated, the mixture was photoirradiated for 15 min and then the photocatalyst was recovered by filtration, and the solution was transferred to ESR analysis.

2.3. Photocatalytic hydrogen production

The photocatalytic H₂ evolving experiments were conducted in an on-line photocatalytic hydrogen production system (LabSolar-3AG, PerfectLight, Beijing). Typically, 10 mg catalysts were suspended in a mixture solution of 80 mL distilled water, 20 mL triethanolamine and 3 wt.% H₂PtCl₆. A 300W Xenon lamp (PLS-SXE 300C (BF)), equipped with a 420-nm cut-off filter was used as the light irradiation source. Gas evolution was analyzed by an on-line gas chromatograph (GC D7900 P, TCD detector).

2.4. Density functional theory calculation

Calculations were performed using the CASTEP code [39], based on density functional theory (DFT) using the plane-wave pseudopotential method, and the generalized-gradient approximation of Perdew, Burke, Ernzerhof (PBE-GGA) [40] for exchange correlation. The electron wave function was expanded in plane waves with a cutoff energy of 340 eV. For the smallest g-C₃N₄ supercell, a 7 × 7 × 1 Monkhorst-Pack grid [41] was used for irreducible Brillouin zone sampling. For the larger supercells, a 3 × 3 × 1 grid was used. Test calculations show that using more k-points does not lead to evident changes in the energetic convergence, electronic band structures and density maps for the electronic states. The total energy is converged to 1.0 × 10⁻⁵ eV/atom, and all the geometries are fully relaxed until the quantum mechanical forces acting on the atoms become less than 0.03 eV/Å.

3. Results and discussion

The microstructures of bulk g-C₃N₄ (CN), CN-SP and CN-SPO nanosheets are schematically shown in Fig. 1a-c. The bulk CN made from melamine is tightly stacked with many layers of nitrogen bridged heptazine units with a thickness over 250 nm, as determined by the atomic force microscopy (AFM) imaging. On the other hand, the CN-SP exhibits a lower thickness of ~150 nm. Importantly, the re-annealing of the latter product not only results in O doping, but also exfoliates the g-C₃N₄ into ~3 nm thick sheets (Fig. 1f, i). According to the height profile, the ultrathin g-C₃N₄ nanosheets exhibit sharp edges and flat surface, suggesting the well-defined 2D geometry, which is beneficial to photocatalytic reactions since more active sites can be exposed.

TEM images (Fig. 2) also prove that the thickness of the g-C₃N₄ samples is gradually reduced by the O-doping procedure. The bulk g-C₃N₄ and the (S, P) doped g-C₃N₄ present as large aggregates that are irregularly stacked together by flakes, as shown in Fig. 2a and b, respectively. Upon the next-step O doping process, the product demonstrates ultrathin nanosheet morphology (Fig. 2c). EDX elemental

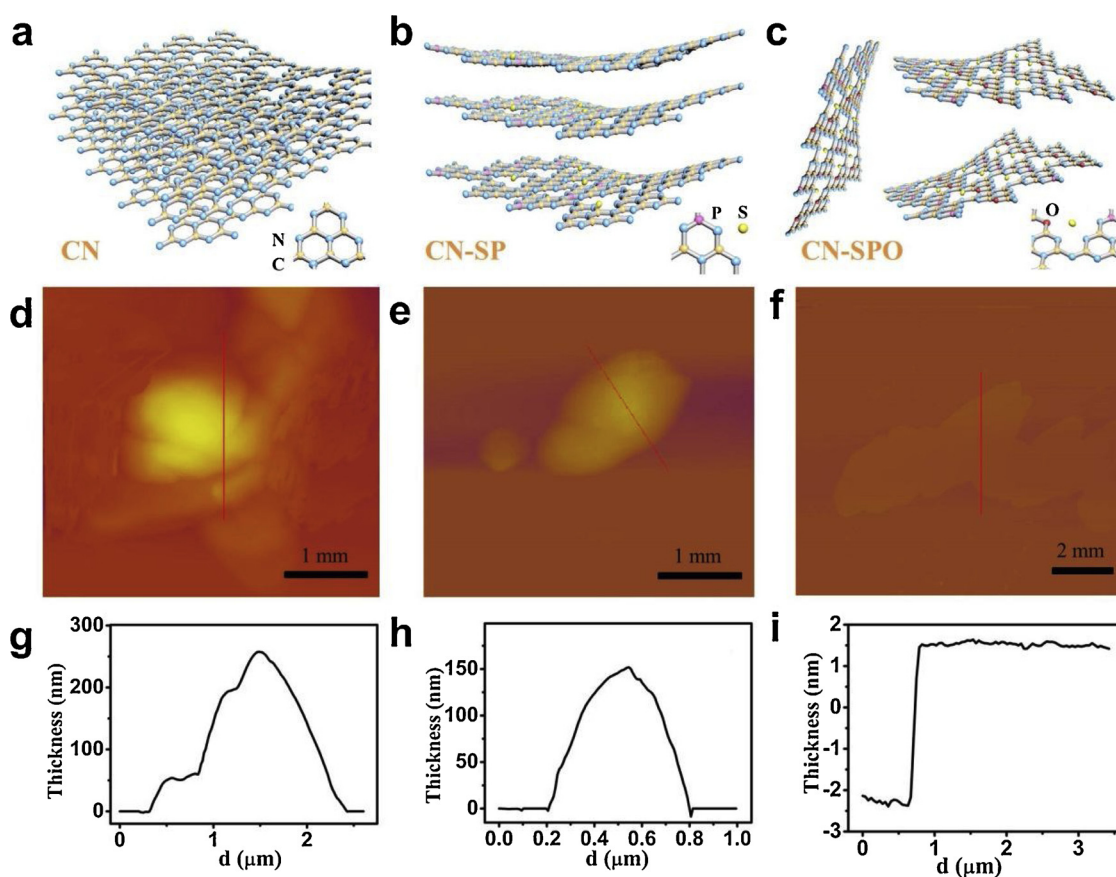


Fig. 1. Schematic illustration of exfoliation procedure of g-C₃N₄ from (a) CN to (b) CN-SP and (c) CN-SPO; AFM images (d–f) and height profile (g–i) of CN (d and g), CN-SP (e and h) and CN-SPO (f and i).

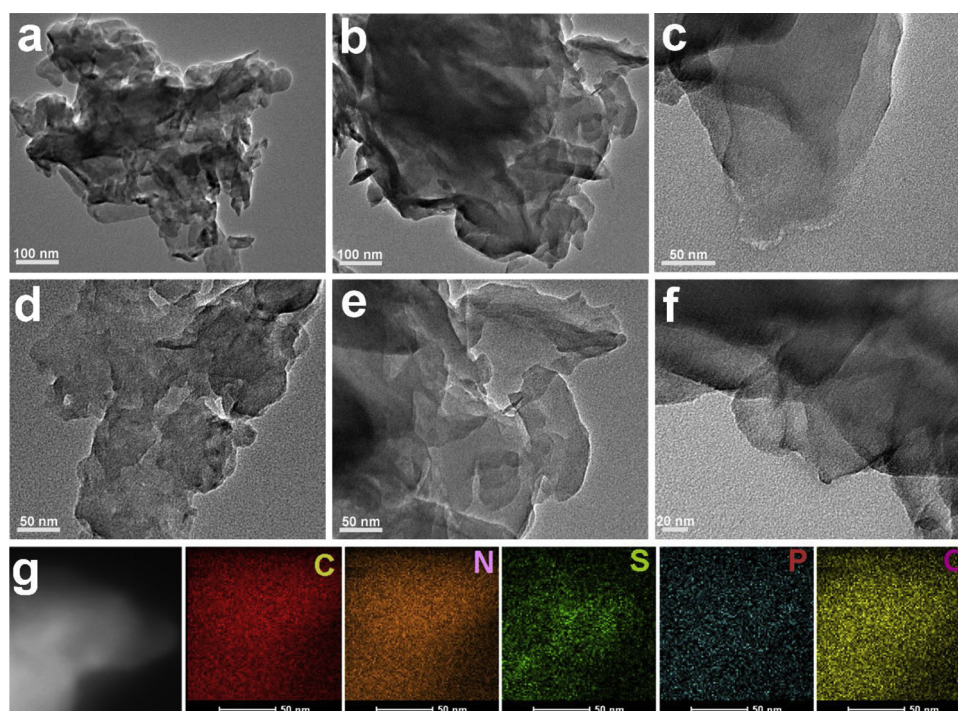


Fig. 2. TEM images of CN (a and d), CN-SP (b and e) and CN-SPO (c and f), (g) TEM image and corresponding EDX-mapping of C, N, S, P, O elements of the CN-SPO sample.

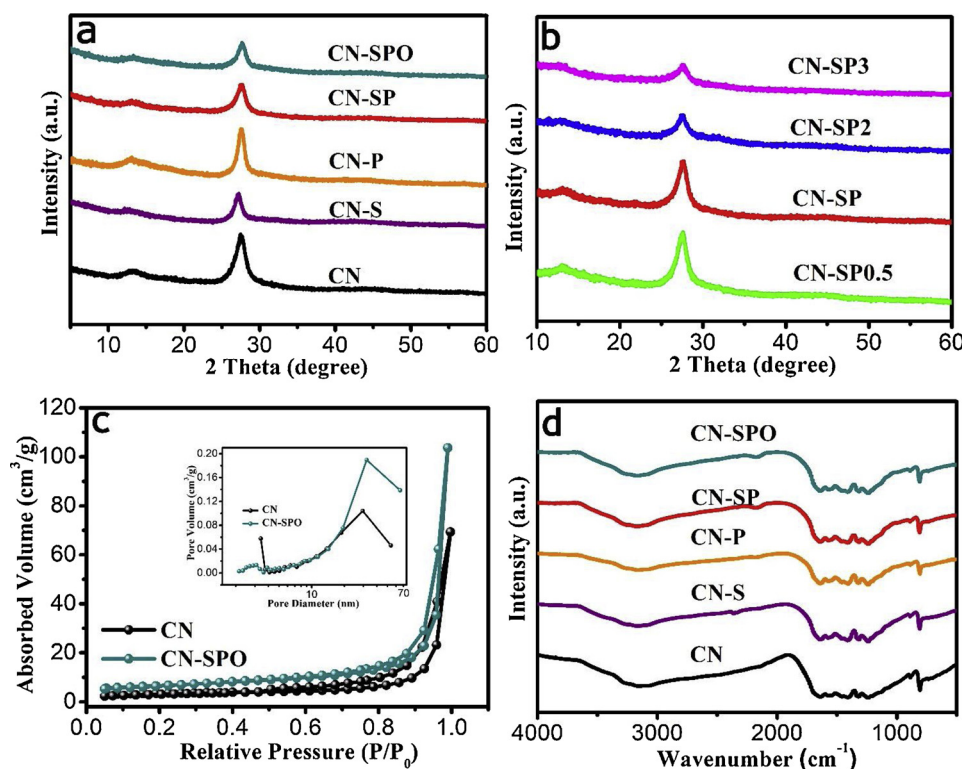


Fig. 3. XRD patterns (a, b), N₂ adsorption-desorption isotherms (c) and FT-IR spectra (d) of CN and doped CN samples.

mappings show that C, N, S, P and O are homogeneously distributed in the CN-SPO sample, indicating the successful doping of multiple elements.

To study the influence of P, S, O doping on the crystal structure of the as-prepared samples, powder X-ray diffraction (XRD) measurements were carried out (Fig. 3a–b). The diffraction peak at 13.1° (2θ) arises from the in-plane structural packing motif of aromatic rings and the peak at 27.1° (002) corresponds to the interlayer-stacking of the g-C₃N₄ layered structure [42,43], indicating that the original crystal structure of g-C₃N₄ is largely retained after doping with different nonmetal elements. In addition, the intensity of the (002) peak decreases with the increase of substituted elements (Fig. 3a) or increasing doping P content (Fig. 3b), demonstrating that the layered g-C₃N₄ can be exfoliated by such doping procedure [44]. This is consistent with the observations from AFM and TEM images. The exfoliating process usually results in an increase in specific surface area. Accordingly, N₂ adsorption-desorption curves were measured for g-C₃N₄ and CN-SPO (Fig. 3c). It can be found that both curves demonstrate a typical IV hysteresis loop and a broad pore-size distribution with mesopores and macropores based on the Barrett-Joyner-Halenda (BJH) method, suggesting the existence of a mesoporous structure. As expected, the surface area of the CN-SPO (23.2 m²/g) is almost 2 times of bulk CN (12.3 m²/g).

The chemical structures of the g-C₃N₄ and samples doped with different nonmetal elements nanosheets were further investigated by the FT-IR spectra (Fig. 3d). For all samples, the peak appeared at 807 cm⁻¹ belongs to the characteristic breathing mode of the heptazine unit, while the signals at 1247, 1324, 1401, 1574, and 1641 cm⁻¹ corresponds to the stretching vibration bands of the C–N heterocycle [45], indicating that the doping samples keep the same chemical structure as their parent bulk g-C₃N₄, which is essential for π–delocalized electronic systems to generate and transport photo-excited electron-hole pairs for the subsequent redox reactions.

XPS measurement was conducted in combination with density functional theory (DFT) calculations to investigate the doping sites of S, P and O in the CN-SPO sample. Fig. 4a shows the XPS survey spectra of bulk CN and CN-SPO. The binding energies for C 1s, N 1s and O 1s can

be observed for both samples, while the P 2p peak only appears in the CN-SPO sample and the S element is not seen in the survey spectrum of CN-SPO sample which may due to the low content. The high resolution C 1s spectra (Fig. 4b) of the two samples can be deconvoluted into two peaks at binding energies of 284.61 and 287.93 eV, which can be ascribed to surface adventitious carbon and sp² hybridized carbon in N=C–N, respectively [46,47]. The N 1s spectra display C–N=C bonding, tertiary N bonds in N–(C)₃ groups and C–N–H functional group at 398.51, 399.85 and 401.04 eV, respectively (Fig. 4c) [48,49]. In addition, the bulk CN and CN-SPO samples exhibit C1s and N1s signals with a C/N ratio of 0.71 and 0.66, respectively. In both cases, the C signals are lower than the theoretical value (0.75) due to the existence of the C vacancy. Firstly, S and P position should be determined because the C N-S PO sample was derived from the CN-SP sample. According to the XPS spectra, the S 2p spectrum of CN-SPO presents two peaks at 164.2 eV and 166.1 eV, respectively, corresponding to the S=N and N–S bonds (Fig. 4d); while the P 2p spectrum of CN-SPO can be deconvoluted into three peaks (Fig. 4e), including P=N bond (132.8 eV), P–N bond (133.6 eV) and P=O bond (134.6 eV) [50].

According to the DFT calculation results (Fig. 5a) based on the perfect crystal of the g-C₃N₄, there are two kinds of possible occupying positions for impurity atom, namely substitutional site and interstitial sites. The substituted doping of P atoms preferentially occur on the C atoms or occupy the interstitial sites of in-planar g-C₃N₄, whereas the S or O doping atoms could achieve the replacement of N atoms or take over the interstitial sites. Based on the XPS results, if S atom replaces the N sites, then S–C bonds should exist in the CN-SPO sample. However, the observation of the N–S bonds indicates that the S atoms occupy the interstitial sites of in-planar g-C₃N₄. Similarly, the existence of P–N bond based on the XPS suggests that P atoms may replace C atoms or occupy the interstitial sites of in-planar g-C₃N₄. Due to the existence of the C vacancy the P atoms are supposed to substitute the C atoms and thus form strong bonds with adjacent N atoms. Although it seems likely that all doping elements tend to occupy interstitial sites due to the lower formation energy (*E_f*), the formation energy for each doping

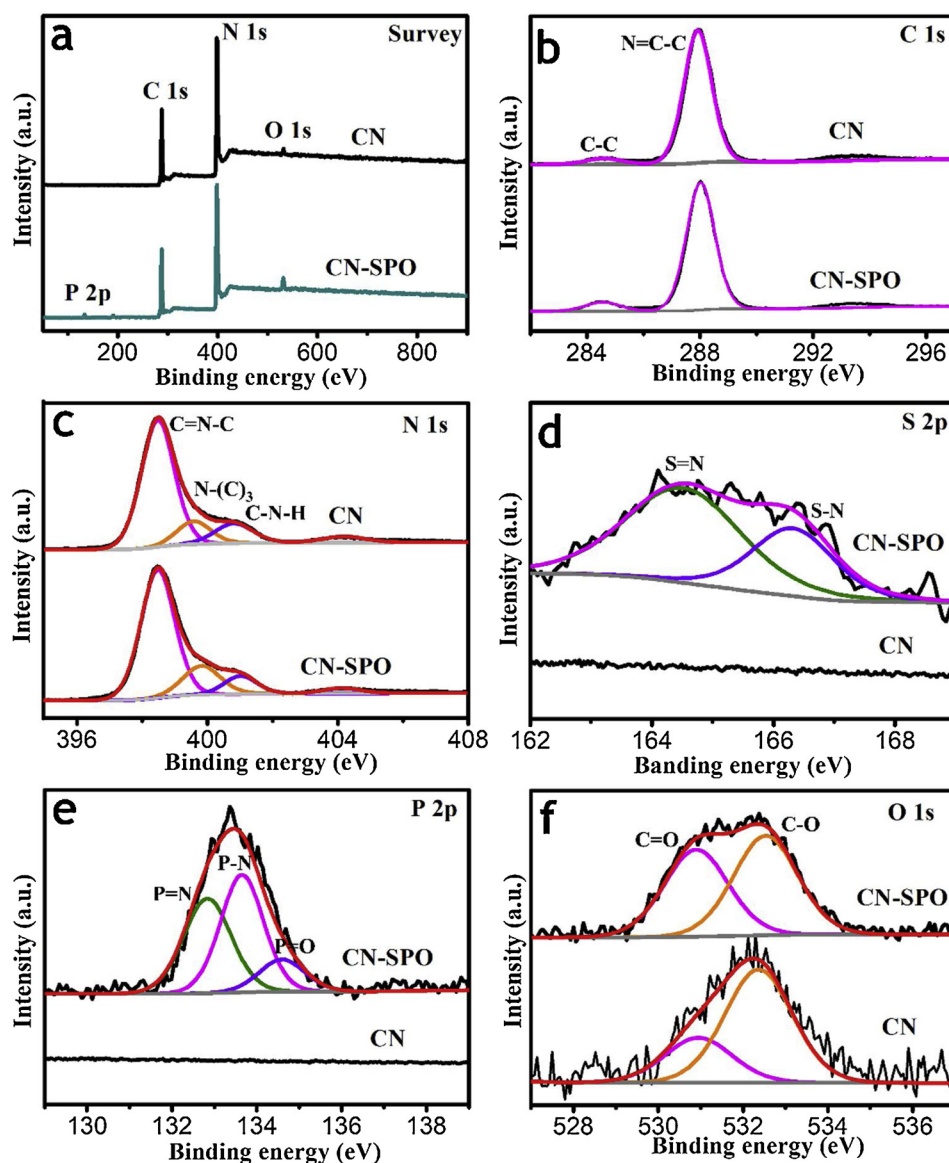


Fig. 4. XPS spectra of CN and doped CN-SPO: (a) survey, (b) C 1s, (c) N 1s, (d) S 2p, (e) P 2p and (f) O 1s.

situation calculation is based on the assumption of perfect $g\text{-C}_3\text{N}_4$ crystals. However, CN-SPO sample with C vacancies does not exhibit a perfect crystal structure, and the sintering process also offers an energy for the substitution of substitutes over C or N elements. Therefore, the substitution of P atoms for C sites and S atom in the interstitial sites are finally determined by the electron density of states via XPS spectrum and DFT calculation.

As for the chemical bonding behavior in $g\text{-C}_3\text{N}_4$, we simply performed the corresponding Mulliken charge and difference charge density maps to analyze the bonding character quantitatively. The Mulliken charge populations corresponding to the overlap of the electron density of P and N atoms are shown in Fig. 6, it can be seen that the transferred Mulliken charge from a P to round N atoms is about 0.644 e when P is at the interstitial sites, and the electron density around P does not overlap with N. Therefore, the strength of P–N bond would be very weak. However, the transferred Mulliken charge from a P to round N atoms is about 1.750 e when P atom exists in the vacancy of C, and the electrons density around P overlap with N to form a strong P–N bond, which is accordance with the XPS result.

The Mulliken charge populations corresponding to the overlap of the electron density of S and N atoms are shown in Fig. 7, the

transferred Mulliken charge from a S to neighboring atoms is 0.590 e and 0.460 e when S is in interstitial site and N in vacancy site, respectively. Accordingly, S forms weak S–N bonds in the interstitial site while no S–N bond exists when S atoms take over the N vacancies. So it is believed that the weak S–N bond should be formed when S is in interstitial site. Because the density of electrons is basically not overlapping, the formation of S–N bond is not as strong as that of the P–N bond. XPS experiments also verified that P replaces C vacancy to form a strong P–N bond and S exists in the interstitial sites to form a weak S–N bond. Finally, the O atom positions are determined. According to the O 1s spectra (Fig. 4f), two peaks at 532.52 eV and 530.88 eV are ascribed to adsorbed hydroxyl group and the latter is ascribed to C–O or C=O, respectively [51]. The intensity of C–O/C=O bond in the CN-SPO sample significantly increases compared with that of bulk CN, suggesting that O atoms have been doped into $g\text{-C}_3\text{N}_4$ and thus more C–O/C=O bonds are formed in the CN-SPO sample. Besides, the formation of C–O indicates the doped O atoms substitutes the N atoms and thus forming bonds with adjacent C atoms.

Under these circumstances, the interstitial S atoms have positive values, indicating that it is an electron donor, while the adjacent two N atoms could have more negative values and are electron acceptors.

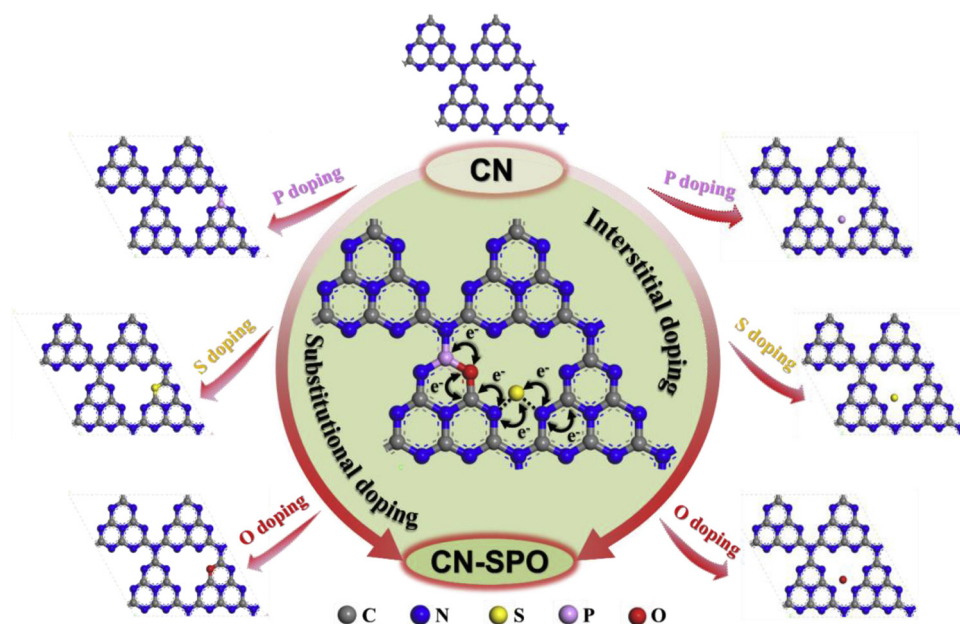


Fig. 5. Schematic illustration of P (or S/O) doped monolayer g-C₃N₄ atomic structures with substitutional-doped sites (left) and interstitial-doped sites (right); the pathway for electron transport and proposed doping sites for the S, P and O atoms from DFT calculations are shown in the middle.

Therefore, the photoexcited electrons can transfer through the O–P–C–N₂–S–N₂' (or N₂'–S–N₂–C₁–P–O) chain (shown in Fig. 5) between two adjacent heptazine units in the S interstitial state, thereby promoting the migration of carriers. Consequently, the delocalized electrons provided by P, O and S are excited and transferred under simulated solar light irradiation, resulting in photocatalytic activity of g-

C₃N₄. Additionally, the band gap structures of the bulk CN and the heteroatoms (S, P and O) doped g-C₃N₄ were calculated for two possible occupying positions (substitutional-doped or interstitial-doped). As shown in Fig. 8, the band gap of bulk CN is 1.18 eV due to the monolayer structure [52] and the band gap of the doped g-C₃N₄ can be reduced no matter which doping is adopted, suggesting that doping is an

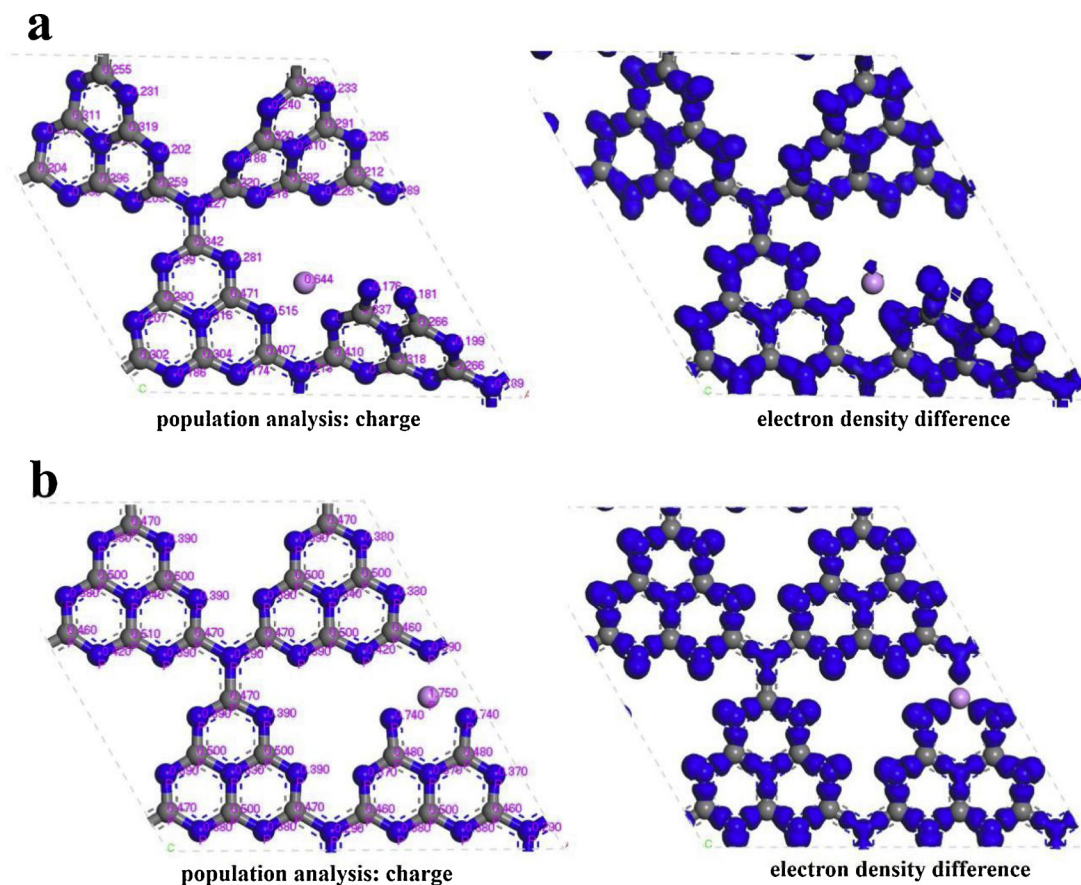


Fig. 6. Mulliken charge populations and electron density difference maps for P in the (a) interstitial site and (b) C substitutional site.

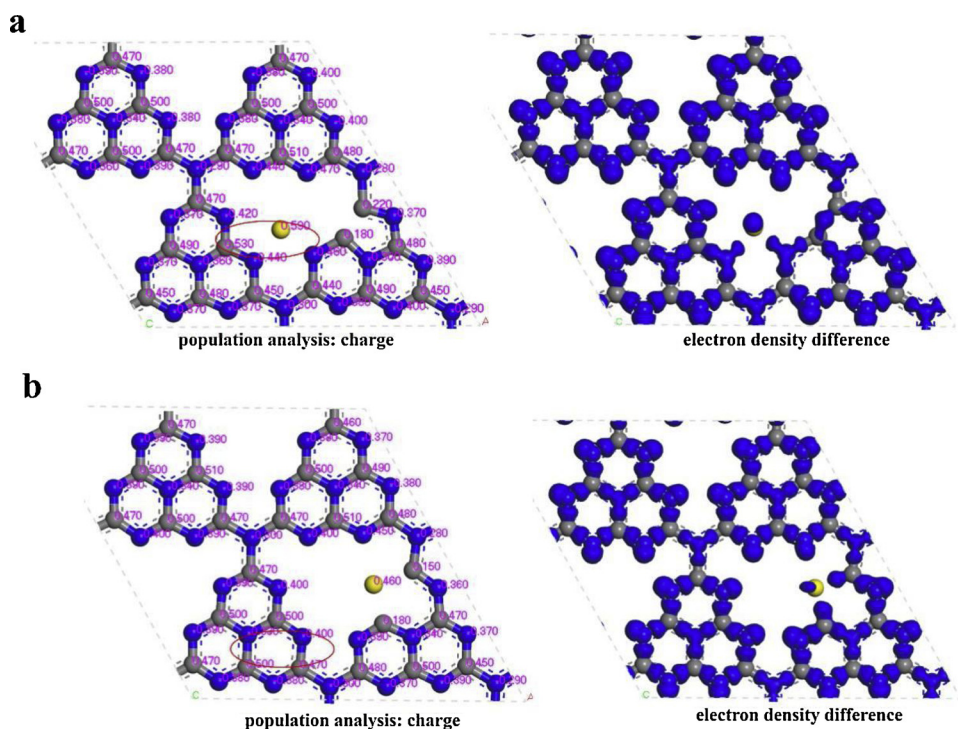


Fig. 7. Mulliken charge populations and electron density difference maps for S in the (a) interstitial site and (b) N substitutional site.

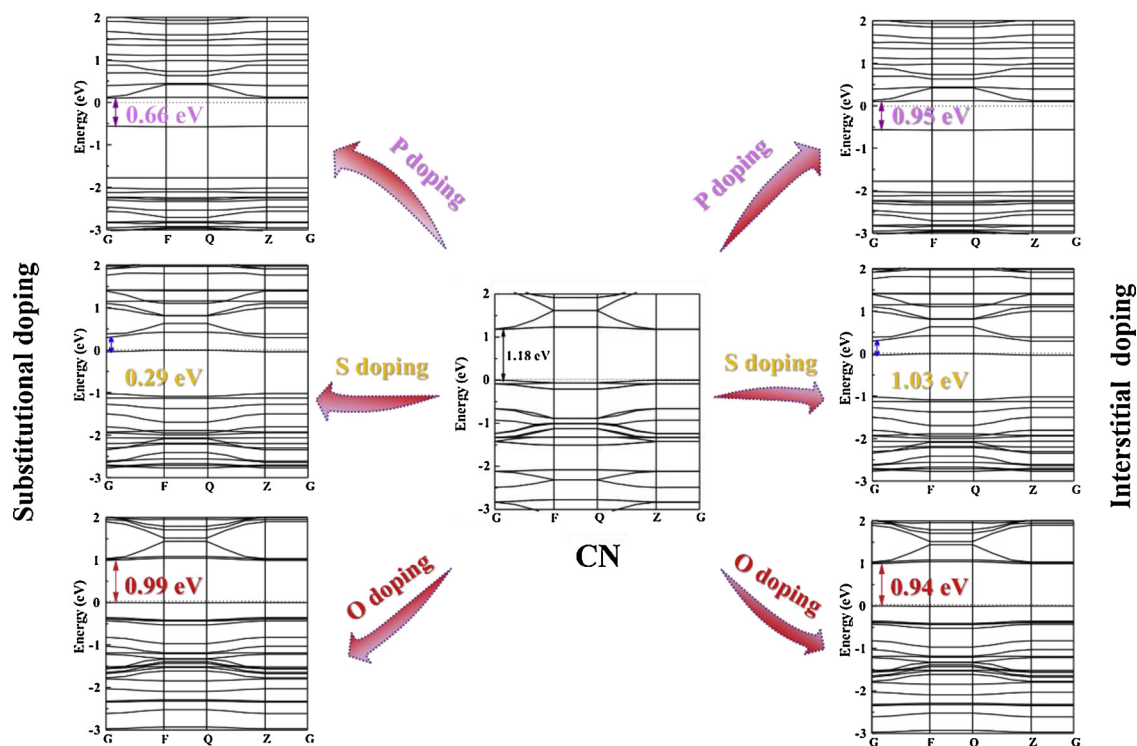


Fig. 8. Calculated band structure of P/S/O for substitutional-doped and interstitial-doped monolayer g-C₃N₄; and the short dash line set at zero is treated as the Fermi level.

effective route to adjust the electronic structure of the g-C₃N₄.

To evaluate the doping effect on the photocatalytic activity, the photocatalytic hydrogen generation was carried out under visible-light irradiation. Fig. 9 illustrates the photocatalytic H₂ evolution over g-C₃N₄ samples with different doping elements and doping concentrations. Bulk CN shows a photocatalytic H₂ evolution of 1402 $\mu\text{mol g}^{-1}$ after 3 h reaction, and doping of only S and only P lead to an increase of

H₂ evolution to 1722 and 3424 $\mu\text{mol g}^{-1}$, respectively. Compared with the single element (S or P) doping, the (S, P) codoped sample (CN-SP) shows a further enhanced H₂ generation activity of 4463 $\mu\text{mol g}^{-1}$.

In addition, the H₂ evolution rate of the g-C₃N₄ increases with increasing P doping concentration, and the CN-SP sample with optimum P doping content exhibits hydrogen evolution rate of 1503 $\mu\text{mol g}^{-1} \text{h}^{-1}$, which is about 1.3 times than that of CN-P

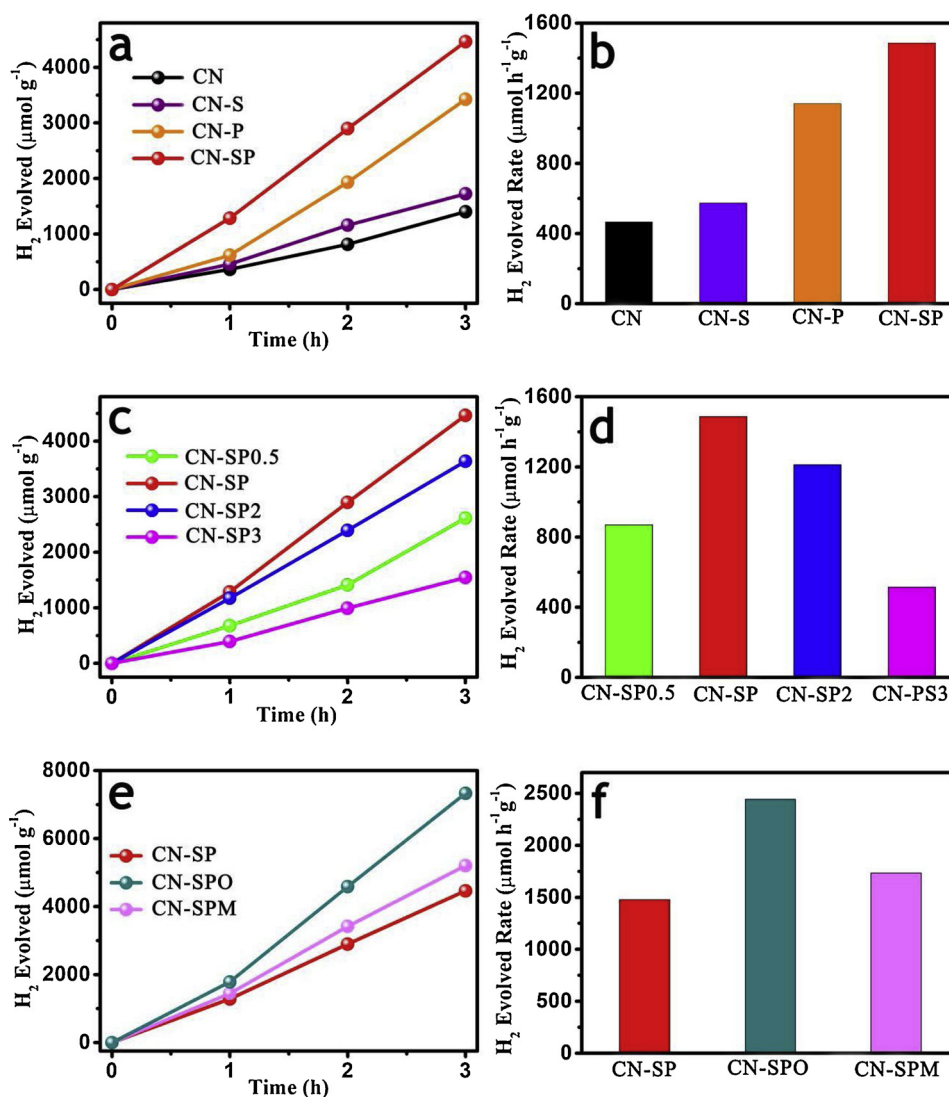


Fig. 9. Evolved hydrogen (a, c, e) and hydrogen-producing rates (b, d, f) over as-prepared photocatalysts under visible-light irradiation ($\lambda > 420$ nm).

(1158 $\mu\text{mol g}^{-1} \text{h}^{-1}$) or 2.5 times than that of CN (586 $\mu\text{mol g}^{-1} \text{h}^{-1}$) (Fig. 9c and d). After annealing the CN-SP sample in air for two times, the CN-SPO sample demonstrates further enhancement of the photocatalytic activity, and 7330 $\mu\text{mol g}^{-1}$ of H_2 was produced after 3 h illumination. In this work, the highest H_2 production rate (2479 $\mu\text{mol g}^{-1} \text{h}^{-1}$) was realized in this CN-SPO sample, which is about 5.3 times higher than that of pure $\text{g-C}_3\text{N}_4$ (465 $\mu\text{mol g}^{-1} \text{h}^{-1}$). The enhanced photocatalytic H_2 production was explained as aforementioned that the photoexcited electrons can transfer through the $\text{O-P-C-N}_2\text{-S-N}_2'$ (or $\text{N}_2'\text{-S-N}_2\text{-C}_1\text{-P-O}$) chain between two adjacent heptazine unit to accelerate the separation of the photogenerated carriers.

To explore the charge separation process, transient photocurrent responses and the EIS Nyquist plots of the samples were measured and recorded. It can be seen that the CN-SPO exhibits the highest photocurrent response (8 $\mu\text{A}/\text{cm}^2$), indicating that the CN-SPO has the optimal separation rate of photogenerated carriers under the visible light irradiation (Fig. 10a). In addition, CN-SPO shows the smallest semicircle radius compared to other samples, indicating the fastest charge-transfer rate in the CN-SPO sample, as smaller semicircle means lower charge-transfer resistance [53,54]. Moreover, photoluminescence (PL) spectra and time-resolved PL spectra are powerful tools to characterize the recombination of photogenerated charge carrier transfer [55]. Both samples (Fig. 10c) exhibit strong PL peak at 450 nm and the PL intensity of bulk CN is higher than that of CN-SPO, indicating more efficient

separation of the charge carriers in CN-SPO sample. Time-resolved PL spectra (Fig. 10d) show that the average lifetime for the CN-SPO sample is lower than that of the bulk CN, also implying the fast electron-hole separation and transport in the CN-SPO sample.

The increase in the efficiency of photoinduced charge separation is bound to the increase of the amount of available electrons for H_2 reduction reaction. Therefore, the ESR with spin label TEMPO was chosen for testing the electrons and holes generation [56,57]. The reactions of TEMPO with electrons or holes can produce an ESR silent molecule and lead to the decrease in the intensity of ESR signals, a sharp decrease in the intensity of TEMPO signals implies that more efficient electrons or holes are produced under light illumination. Both the ESR spectra (Fig. 10e and f) of TEMPO- e^- and TEMPO- h^+ exhibit three signal peaks with intensity of 1:1:1. Compared to the dark condition, the ESR intensities of the TEMPO- e^- and TEMPO- h^+ are greatly reduced for both samples after light on, indicating that electrons and holes are produced from photoexcited CN and CN-SPO samples. Almost no TEMPO- e^- signal can be observed for CN-SPO and the intensity of TEMPO- h^+ of the CN-SPO is weaker than that of the CN, indicating that the CN-SPO has a higher reactivity of photoinduced charge carriers. In combination with the photocurrent, EIS, PL and ESR measurements, it can be conferred that the emerging of new channels originated from the heteroatoms (S, P and O) doping can retard the recombination of the photoexcited electron-hole pairs and resulted in more available

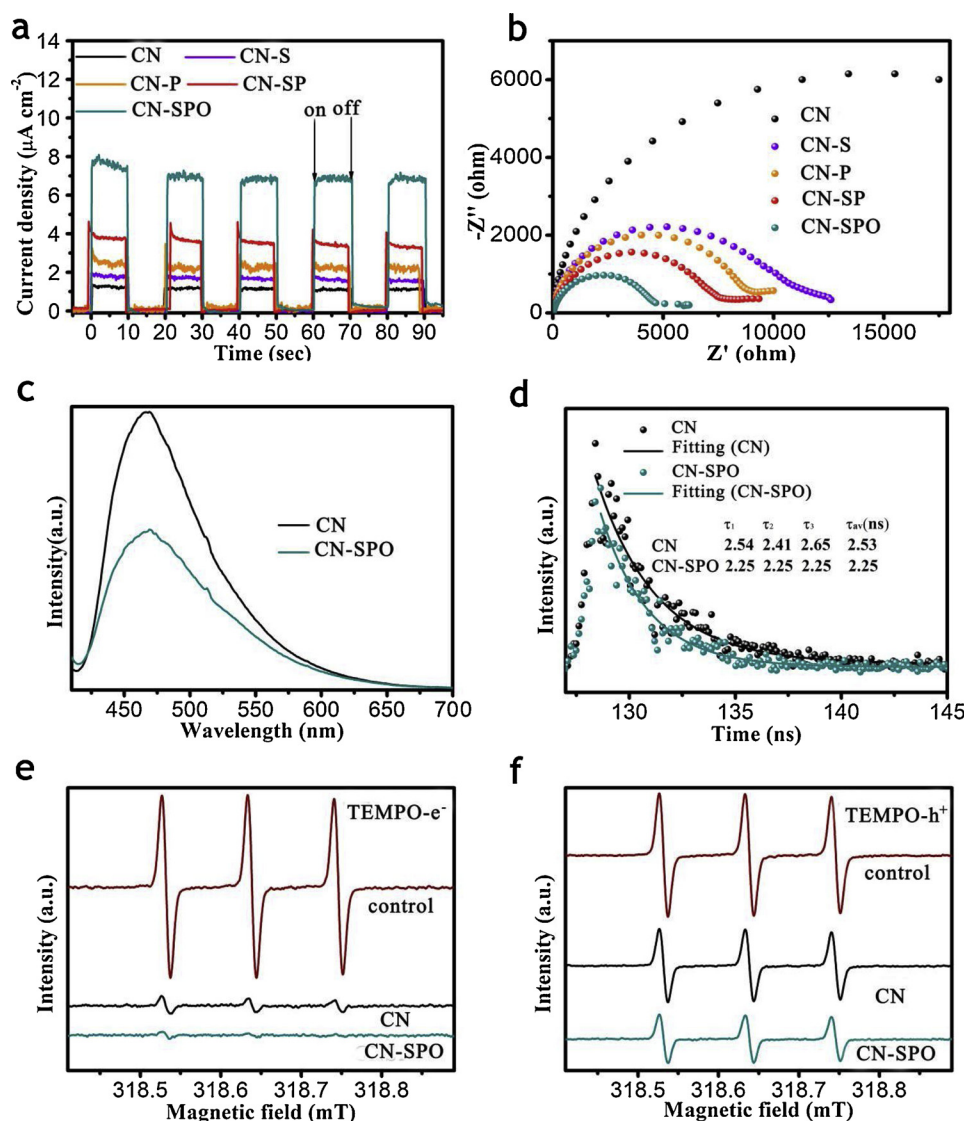


Fig. 10. Photocurrent-time profiles (a), electrochemical impedance spectra (b) of CN and doped CN samples; steady-state (c) and time-resolved (d) PL spectra of CN and CN-SPO; in-situ ESR signals labeled by TEMPO for electrons (e) and holes in CN and CN-SPO dispersions.

electrons for H_2 reduction reaction.

In addition to accelerating the photoinduced charge separation, the doping process can also modulate the band structure and enhance the light absorption or adjust the valance band position to increase the hydrogen evolution ability. Accordingly, the optical property of CN and CN-SPO are characterized using diffuse reflectance spectroscopy (DRS, Fig. 11a). Bulk CN exhibits a typical absorption edge at 460 nm, while CN-SPO shows a redshift of the optical absorption, which is beneficial to the photocatalytic water splitting. The band gap of the CN and CN-SPO are determined to be 2.4 eV and 2.34 eV by plotting the Tauc curves (Fig. 11b). Mott-Schottky curves are applied to determine conduction band (CB) potentials of CN and CN-SPO samples. As shown in Fig. 11c, flat band potentials of CN and CN-SPO samples derived from the intercept of the tangent of the Mott-Schottky curves are -0.56 and -0.64 V (vs Ag/AgCl, pH = 7). According to Ag/AgCl electrode potential [58] and the specific formula $E(\text{NHE}) = E(\text{Ag/AgCl}) - E^\theta + 0.059\text{pH}$, CB potentials of CN and CN-SPO samples are determined to be -0.35 V and -0.43 V, respectively. Based on these results, the bottom CB and the energy band structure of the samples are proposed. As shown in Fig. 11d, the topmost CB of CN-SPO shifts 0.08 V to higher energy (more negative) compared to the CN due to the incorporation of heteroatoms. Meanwhile, the negative

shifting of CB is favorable to the photocatalytic H_2 evolution, because the photogenerated electrons have higher reduction ability in CN-SPO. In light of the above-discussed results, we propose that the enhanced photocatalytic H_2 production activity of the ternary non-metal atoms codoped $\text{g-C}_3\text{N}_4$ is attributed to three factors. The first is that the doping process can reduce the thickness $\text{g-C}_3\text{N}_4$ and enlarge the specific surface area, thereby providing more active sites for hydrogen production. The second is that the interstitial doping of heteroatoms into the $\text{g-C}_3\text{N}_4$ could provide new channels to mediate charge carrier migration through the bridging (S, P, O) atoms, which can boost the charge separation and thus enhance the photocatalytic activity. The third is that both the electronic structure and texture of CN-SPO has been modified to harvest more visible light and more favorable to H_2 reduction reaction.

4. Conclusion

In summary, we presented the simultaneous (S, P, O) doping and exfoliation of the CN-SPO ultrathin 2D nanosheets by a sequential annealing method. Firstly, CN-SP was synthesized through thermal condensation of a homogenous mixture of melamine, thiourea and diammonium phosphate. Afterwards, the as-obtained CN-SP was annealed

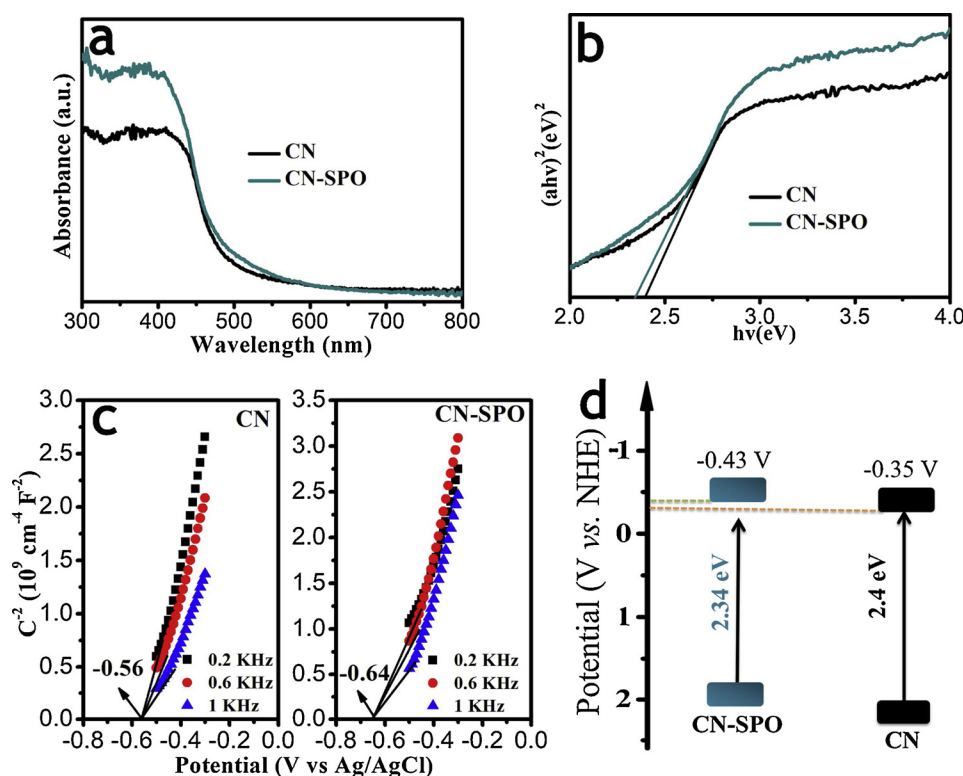


Fig. 11. Diffuse reflectance spectra (a), estimated band gaps (b), Mott-Schottky plots (c) and proposed band structures (d) of CN and CN-SPO.

in air for O doping and concurrently the material was exfoliated into ultrathin, flat nanosheets with a thickness of ~ 3 nm. The CN-SPO nanosheets exhibited increased surface active sites, modulated band structure and enhanced charge transfer upon photo-excitation, leading to significantly improved photocatalytic hydrogen evolution. Under optimized condition, the H_2 evolution rate over the CN-SPO nanosheets reached $2480 \mu\text{mol g}^{-1} \text{h}^{-1}$, which was about 5 times higher than bulk $\text{g-C}_3\text{N}_4$. DFT calculation combined with a series of measurements were carried out to determine the doping sites of the non-metal elements, i.e. S atoms occupied the interstitial sites of the $\text{g-C}_3\text{N}_4$ framework, meanwhile P and O atoms replaced the C and N atoms, respectively. The (S, P, O) doping created a favorable electron transport mode, resulting in retarded charge carrier recombination upon photo-excitation. We believe this work not only develops a highly effective strategy for photocatalyst modification but also sheds light on the working mechanism of the newly developed CN-SPO material.

Acknowledgements

X. Yang acknowledges the financial support from Six Talent Peaks Project in Jiangsu Province (2015-XCL-026), Natural Science Foundation of Jiangsu Province (BK20171299), Startup Funding from Nanjing Forestry University, State Key Laboratory of Photocatalysis on Energy and Environment (SKLPEE-KF201705), Fuzhou University. We are also grateful for financial support from the National Natural Science Foundation of China (51672113), Natural Science Foundation of Jiangsu Province (BK20150480), QingLan Project of Jiangsu Province, Senior Talent Foundation of Jiangsu University (15JD036) and Training Project of Jiangsu University for Young Cadre Teachers (5521220009). J.X. is grateful to Discovery Early Career Researcher Award (DECRA) by Australian Research Council (DE160101488) and State Key Laboratory of Advanced Technology for Materials Synthesis and Processing (Wuhan University of Technology) (2018-KF-17).

References

- [1] J.S. Xu, H. Wang, C. Zhang, X.F. Yang, S.W. Cao, J.G. Yu, M. Shalom, From millimeter to subnanometer: vapor-solid deposition of carbon nitride hierarchical nanostructures directed by supramolecular assembly, *Angew. Chem. Int. Ed.* 56 (2017) 8426–8430.
- [2] P. Niu, L.C. Yin, Y.Q. Yang, G. Liu, H.M. Cheng, Increasing the visible light absorption of graphitic carbon nitride (Melon) photocatalysts by homogeneous self-modification with nitrogen vacancies, *Adv. Mater.* 26 (2014) 8046–8052.
- [3] Y.H. Ao, K.D. Wang, P.F. Wang, C. Wang, J. Hou, Synthesis of novel 2D-2D p-n heterojunction $\text{BiOBr/La}_2\text{TiO}_7$ composite photocatalyst with enhanced photocatalytic performance under both UV and visible light irradiation, *Appl. Catal. B-Environ.* 194 (2016) 157–168.
- [4] Y.Y. Wang, W.J. Yang, X.J. Chen, J. Wang, Y.F. Zhu, Photocatalytic activity enhancement of core-shell structure $\text{g-C}_3\text{N}_4/\text{TiO}_2$ via controlled ultrathin $\text{g-C}_3\text{N}_4$ layer, *Appl. Catal. B-Environ.* 220 (2018) 337–347.
- [5] X.J. She, J.J. Wu, H. Xu, Z. Mo, J.B. Lian, Y.H. Song, L. Liu, D.L. Du, H.M. Li, Enhancing charge density and steering charge unidirectional flow in 2D non-metallic semiconductor-CNTs-metal coupled photocatalyst for solar energy conversion, *Appl. Catal. B-Environ.* 202 (2017) 112–117.
- [6] G. Yang, H. Ding, D.M. Chen, J.J. Feng, Q. Hao, Y.F. Zhu, Construction of urchin-like $\text{ZnIn}_2\text{S}_4\text{-Au-TiO}_2$ heterostructure with enhanced activity for photocatalytic hydrogen evolution, *Appl. Catal. B-Environ.* 234 (2018) 260–267.
- [7] X.C. Wang, K. Maeda, A. Thomas, K. Takanabe, G. Xin, J.M. Carlsson, K. Domen, M. Antonietti, A metal-free polymeric photocatalyst for hydrogen production from water under visible light, *Nat. Mater.* 8 (2009) 76–80.
- [8] G.G. Zhang, G.S. Li, Z.A. Lan, L.H. Lin, A. Savateev, T. Heil, S. Zafeirotas, X.C. Wang, M. Antonietti, Optimizing optical absorption, exciton dissociation, and charge transfer of a polymeric carbon nitride with ultrahigh solar hydrogen production activity, *Angew. Chem. Int. Ed.* 56 (2017) 13445–13449.
- [9] J.W. Sun, J.S. Xu, A. Grafmueller, X. Huang, C. Liedel, G. Algara-Siller, M. Willinger, C. Yang, Y.S. Fu, X. Wang, M. Shalom, Self-assembled carbon nitride for photocatalytic hydrogen evolution and degradation of p-nitrophenol, *Appl. Catal. B-Environ.* 205 (2017) 1–10.
- [10] Y.Y. Wang, W.J. Jiang, W.J. Luo, X.J. Chen, Y.F. Zhu, Ultrathin nanosheets $\text{g-C}_3\text{N}_4/\text{Bi}_2\text{WO}_6$ core-shell structure via low temperature reassembled strategy to promote photocatalytic activity, *Appl. Catal. B-Environ.* 237 (2018) 633–640.
- [11] G. Yang, D.M. Chen, H. Ding, J.J. Feng, J.Z. Zhang, Y.F. Zhu, S. Hamid, D.W. Bahnemann, Well-designed 3D ZnIn_2S_4 nanosheets/ TiO_2 nanobelts as direct Z-scheme photocatalysts for CO_2 photoreduction into renewable hydrocarbon fuel with high efficiency, *Appl. Catal. B-Environ.* 219 (2017) 611–618.
- [12] Y.L. Li, P.P. Li, J.S. Wang, Y.L. Yang, W.Q. Yao, Z. Wei, J.S. Wu, X.X. Yan, X.F. Xu, Y.H. Liu, Y.F. Zhu, Water soluble graphitic carbon nitride with tunable fluorescence for boosting broad-response photocatalysis, *Appl. Catal. B-Environ.* 225 (2018) 519–529.
- [13] J. Liu, Y. Liu, N.Y. Liu, Y.Z. Han, X. Zhang, H. Huang, Y. Lifshitz, S.T. Lee, J. Zhong,

- Z.H. Kang, Metal-free efficient photocatalyst for stable visible water splitting via a two-electron pathway, *Science* 347 (2015) 970–974.
- [14] B. Kurpil, K. Otte, M. Antonietti, A. Savateev, Photooxidation of N-acylhydrazones to 1,3,4-oxadiazoles catalyzed by heterogeneous visible-light-active carbon nitride semiconductor, *Appl. Catal. B-Environ.* 228 (2018) 97–102.
- [15] M. Antonietti, A. Savateev, Heterogeneous organocatalysis for photoredox chemistry, *ACS Catal.* 8 (2018) 9790–9808.
- [16] A. Savateev, I. Ghosh, B. Konig, M. Antonietti, Photoredox catalytic organic transformations using heterogeneous carbon nitrides, *Angew. Chem. Int. Ed.* 57 (2018) 15936–15947.
- [17] A. Savateev, B. Kurpil, A. Mishchenko, G. Zhang, M. Antonietti, “Waiting” carbon nitride radical anion: charge storage material and key intermediate in direct C-H thiolation of methylenes using elemental sulfur as “S”-source, *Chem. Sci.* 9 (2018) 3584–3591.
- [18] Z.F. Jiang, W.M. Wan, H.M. Li, S.Q. Yuan, H.J. Zhao, P.K. Wong, A hierarchical Z-scheme $\alpha\text{-Fe}_2\text{O}_3/\text{g-C}_3\text{N}_4$ hybrid for enhanced photocatalytic CO_2 reduction, *Adv. Mater.* 30 (2018) 1706108.
- [19] X.J. She, J.J. Wu, H. Xu, J. Zhong, Y. Wang, Y.H. Song, K.Q. Nie, Y. Liu, Y.C. Yang, M.T.F. Rodrigues, R. Vajtai, J. Lou, D.L. Du, H.M. Li, P.M. Ajayan, High efficiency photocatalytic water splitting using 2D $\alpha\text{-Fe}_2\text{O}_3/\text{g-C}_3\text{N}_4$ Z-scheme catalysts, *Adv. Energy Mater.* 7 (2017) 1700025.
- [20] H.X. Shao, X. Zhao, Y.B. Wang, R. Mao, Y. Wang, M. Qiao, S. Zhao, Y.F. Zhu, Synergetic activation of peroxymonosulfate by Co_3O_4 modified $\text{g-C}_3\text{N}_4$ for enhanced degradation of diclofenac sodium under visible light irradiation, *Appl. Catal. B-Environ.* 218 (2017) 810–818.
- [21] X. Wang, Y.H. Liang, W.J. An, J.S. Hu, Y.F. Zhu, W.Q. Cui, Removal of chromium (VI) by a self-regenerating and metal free $\text{g-C}_3\text{N}_4$ /graphene hydrogel system via the synergy of adsorption and photo-catalysis under visible light, *Appl. Catal. B-Environ.* 219 (2017) 53–62.
- [22] H.J. Yu, R. Shi, Y.X. Zhao, T. Bian, Y.F. Zhao, C. Zhou, G.I.N. Waterhouse, L.Z. Wu, C.H. Tung, T.R. Zhang, Alkali-assisted synthesis of nitrogen deficient graphitic carbon nitride with tunable band structures for efficient visible-light-driven hydrogen evolution, *Adv. Mater.* 29 (2017) 1605148.
- [23] H.J. Yu, L. Shang, T. Bian, R. Shi, G.I.N. Waterhouse, Y.F. Zhao, C. Zhou, L.Z. Wu, C.H. Tung, T.R. Zhang, Nitrogen-doped porous carbon nanosheets templated from $\text{g-C}_3\text{N}_4$ as metal-free electrocatalysts for efficient oxygen reduction reaction, *Adv. Mater.* 28 (2016) 5080–5086.
- [24] W.D. Oh, V.W.C. Chang, Z.T. Hu, R. Goei, T.T. Lim, Enhancing the catalytic activity of $\text{g-C}_3\text{N}_4$ through Me doping (Me = Cu, Co and Fe) for selective sulfathiazole degradation via redox-based advanced oxidation process, *Chem. Eng. J.* 323 (2017) 260–269.
- [25] Y.Y. Kang, Y.Q. Yang, L.C. Yin, X.D. Kang, L.Z. Wang, G. Liu, H.M. Cheng, Selective breaking of hydrogen bonds of layered carbon nitride for visible light photocatalysis, *Adv. Mater.* 28 (2016) 6471–6478.
- [26] G. Liu, P. Niu, C.H. Sun, S.C. Smith, Z.G. Chen, G.Q. Lu, H.M. Cheng, Unique electronic structure induced high photoreactivity of sulfur-doped graphitic C_3N_4 , *J. Am. Chem. Soc.* 132 (2010) 11642–11648.
- [27] J. Wang, Z. Yang, X.X. Gao, W.Q. Yao, W.Q. Wei, X.J. Chen, R.L. Zong, Y.F. Zhu, Core-shell $\text{g-C}_3\text{N}_4/\text{ZnO}$ composites as photoanodes with double synergistic effects for enhanced visible-light photoelectrocatalytic activities, *Appl. Catal. B-Environ.* 217 (2017) 169–180.
- [28] S.C. Yan, Z.S. Li, Z.G. Zou, Photodegradation of Rhodamine B and methyl orange over boron-doped $\text{g-C}_3\text{N}_4$ under visible light irradiation, *Langmuir* 26 (2010) 3894–3901.
- [29] Y. Wang, Y. Di, M. Antonietti, H.R. Li, X.F. Chen, X.C. Wang, Excellent visible-light photocatalysis of fluorinated polymeric carbon nitride solids, *Chem. Mater.* 22 (2010) 5119–5121.
- [30] X.G. Ma, Y.H. Lv, J. Xu, Y.F. Liu, R.Q. Zhang, Y.F. Zhu, A strategy of enhancing the photoactivity of $\text{g-C}_3\text{N}_4$ via doping of nonmetal elements: a First-Principles Study, *J. Phys. Chem. C* 116 (2012) 23485–23493.
- [31] C.C. Hu, W.Z. Hung, M.S. Wang, P.J. Lu, Phosphorus and sulfur codoped $\text{g-C}_3\text{N}_4$ as an efficient metal-free photocatalyst, *Carbon* 127 (2018) 374–383.
- [32] S.W. Cao, Q. Huang, B.C. Zhu, J.G. Yu, Trace-level phosphorus and sodium co-doping of $\text{g-C}_3\text{N}_4$ for enhanced photocatalytic H_2 production, *J. Power Sources* 351 (2017) 151–159.
- [33] J.J. Wu, N. Li, X.H. Zhang, H.B. Fang, Y.Z. Zheng, X. Tao, Heteroatoms binary-doped hierarchical porous $\text{g-C}_3\text{N}_4$ nanobelts for remarkably enhanced visible-light-driven hydrogen evolution, *Appl. Catal. B-Environ.* 226 (2018) 61–70.
- [34] B.C. Zhu, J.F. Zhang, C.J. Jiang, B. Cheng, J.G. Yu, First principle investigation of halogen-doped monolayer $\text{g-C}_3\text{N}_4$ photocatalyst, *Appl. Catal. B-Environ.* 207 (2017) 27–34.
- [35] J.J. Ji, J. Wen, Y.F. Shen, Y.Q. Lv, Y.L. Chen, S.Q. Liu, H.B. Ma, Y.J. Zhang, Simultaneous noncovalent modification and exfoliation of 2D carbon nitride for enhanced electrochemiluminescent biosensing, *J. Am. Chem. Soc.* 139 (2017) 11698–11701.
- [36] J.G. Cui, D.W. Qi, X. Wang, Research on the techniques of ultrasound-assisted liquid-phase peeling, thermal oxidation peeling and acid-base chemical peeling for ultra-thin graphite carbon nitride nanosheets, *Ultrason. Sonochem.* 48 (2018) 181–187.
- [37] X.D. Zhang, H.X. Wang, H. Wang, Q. Zhang, J.F. Xie, Y.P. Tian, J. Wang, Y. Xie, Single-layered graphitic- C_3N_4 quantum dots for two-photon fluorescence imaging of cellular nucleus, *Adv. Mater.* 26 (2014) 4438–4444.
- [38] X.J. She, J.J. Wu, J. Zhong, H. Xu, Y.C. Yang, R. Vajtai, J. Lou, Y. Liu, D.L. Du, H.M. Li, P.M. Ajayan, Oxygenated monolayer carbon nitride for excellent photocatalytic hydrogen evolution and external quantum efficiency, *Nano Energy* 27 (2016) 138–146.
- [39] S.J. Clark, M.D. Segall, C.J. Pickard, P.J. Hasnip, M.J. Probert, K. Refson, M.C. Payne, First principles methods using CASTEP, *Z. Kristallogr.* 220 (2005) 567–570.
- [40] J.P. Perdew, A. Ruzsinszky, G.I. Csonka, O.A. Vydrov, G.E. Scuseria, L.A. Constantin, X.L. Zhou, K. Burke, Restoring the density-gradient expansion for exchange in solids and surfaces, *Phys. Rev. Lett.* 100 (2008) 136406.
- [41] L.O. Wagner, E.M. Stoudenmire, K. Burke, S.R. White, Guaranteed convergence of the kohn-sham equations, *Phys. Rev. Lett.* 111 (2013) 093003.
- [42] S.W. Cao, H. Li, T. Tong, H.C. Chen, A.C. Yu, J.G. Yu, H.M. Chen, Single-atom engineering of directional charge transfer channels and active sites for photocatalytic hydrogen evolution, *Adv. Funct. Mater.* 28 (2018) 1802169.
- [43] Z. Mo, H. Xu, Z.G. Chen, X.J. She, Y.H. Song, J.J. Wu, P.C. Yan, L. Xu, Y.C. Leia, S.Q. Yuan, H.M. Li, Self-assembled synthesis of defect-engineered graphitic carbon nitride nanotubes for efficient conversion of solar energy, *Appl. Catal. B-Environ.* 225 (2018) 154–161.
- [44] J.R. Ran, T.Y. Ma, G.P. Gao, X.W. Du, S.Z. Qiao, Porous P-doped graphitic carbon nitride nanosheets for synergistically enhanced visible-light photocatalytic H_2 production, *Energy Environ. Sci.* 8 (2015) 3708–3717.
- [45] H.W. Huang, K. Xiao, N. Tian, F. Dong, T.R. Zhang, X. Du, Y.H. Zhang, Template-free precursor-surface-etching route to porous, thin $\text{g-C}_3\text{N}_4$ nanosheets for enhancing photocatalytic reduction and oxidation activity, *J. Mater. Chem. A* 5 (2017) 17452–17463.
- [46] N. Tian, Y.H. Zhang, X.W. Li, K. Xiao, X. Du, F. Dong, G.I.N. Waterhouse, T.R. Zhang, H.W. Huang, Precursor-reforming protocol to 3D mesoporous $\text{g-C}_3\text{N}_4$ established by ultrathin self-doped nanosheets for superior hydrogen evolution, *Nano Energy* 38 (2017) 72–81.
- [47] H. Xu, J.J. Yi, X.J. She, Q. Liu, L. Song, S.M. Chen, Y.C. Yang, Y.H. Song, R. Vajtai, J. Lou, H.M. Li, S.Q. Yuan, J.J. Wu, P.M. Ajayan, 2D heterostructure comprised of metallic 1T- MoS_2 /Monolayer O-g- C_3N_4 towards efficient photocatalytic hydrogen evolution, *Appl. Catal. B-Environ.* 220 (2018) 379–385.
- [48] Z.P. Chen, S. Mitchell, E. Vorobyeva, R.K. Leary, R. Hauert, T. Furnival, Q.M. Ramasse, J.M. Thomas, P.A. Midgley, D. Dontsova, M. Antonietti, S. Pogodin, N. Lopez, J. Perez-Ramirez, Stabilization of single metal atoms on graphitic carbon nitride, *Adv. Funct. Mater.* 27 (2017) 1605785.
- [49] X. Yang, L. Tian, X. Zhao, H. Tang, Q. Liu, G. Li, Interfacial optimization of $\text{g-C}_3\text{N}_4$ -based Z-scheme heterojunction toward synergistic enhancement of solar-driven photocatalytic oxygen evolution, *Appl. Catal. B-Environ.* 244 (2019) 240–249.
- [50] Y.J. Zhang, T. Mori, J.H. Ye, M. Antonietti, Phosphorus-doped carbon nitride solid: enhanced electrical conductivity and photocurrent generation, *J. Am. Chem. Soc.* 132 (2010) 6294–6295.
- [51] X.J. She, L. Liu, H.Y. Ji, Z. Mo, Y.P. Li, L.Y. Huang, D.L. Du, H. Xu, H.M. Li, Template-free synthesis of 2D porous ultrathin nonmetal-doped $\text{g-C}_3\text{N}_4$ nanosheets with highly efficient photocatalytic H_2 evolution from water under visible light, *Appl. Catal. B-Environ.* 187 (2016) 144–153.
- [52] B.C. Zhu, L.Y. Zhang, B. Cheng, J.G. Yu, First-principle calculation study of tri-s-triazine-based $\text{g-C}_3\text{N}_4$: a review, *Appl. Catal. B-Environ.* 224 (2018) 983–999.
- [53] Q.Q. Liu, J.Y. Shen, X.F. Yang, T.R. Zhang, H. Tang, 3D reduced graphene oxide aerogel-mediated Z-scheme photocatalytic system for highly efficient solar-driven water oxidation and removal of antibiotics, *Appl. Catal. B-Environ.* 232 (2018) 562–573.
- [54] J.Y. Li, H. Xu, Y.G. Xu, Y.H. Song, J.B. Lian, Y. Zhao, L. Wang, L.Y. Huang, H.Y. Ji, H.M. Li, Graphene quantum dots modified mesoporous graphitic carbon nitride with significant enhancement of photocatalytic activity, *Appl. Catal. B-Environ.* 207 (2017) 429–437.
- [55] A.Y. Meng, S. Wu, B. Cheng, J.G. Yu, J.S. Xu, Hierarchical $\text{TiO}_2/\text{Ni(OH)}_2$ composite fibers with enhanced photocatalytic CO_2 reduction performance, *J. Mater. Chem. A* 6 (2018) 4729–4736.
- [56] X.F. Yang, H.Y. Cui, Y. Li, J.L. Qin, R.X. Zhang, H. Tang, Fabrication of Ag_3PO_4 -graphene composites with highly efficient and stable visible light photocatalytic performance, *ACS Catal.* 3 (2013) 363–369.
- [57] L. Tian, X.Z. Xian, X.K. Cui, H. Tang, X.F. Yang, Fabrication of modified $\text{g-C}_3\text{N}_4$ nanorod/ Ag_3PO_4 nanocomposites for solar-driven photocatalytic oxygen evolution from water splitting, *Appl. Surf. Sci.* 430 (2018) 301–308.
- [58] S. Cao, B. Shen, T. Tong, J. Fu, J. Yu, 2D/2D heterojunction of ultrathin MXene/ Bi_2WO_6 nanosheets for improved photocatalytic CO_2 reduction, *Adv. Funct. Mater.* (2018) 1800136.